

Zero-polarization candidate regions for calibration of wide-field optical polarimeters

N. Mandarakas^{1,2,*}, G. V. Panopoulou³, V. Pelgrims⁴, S. B. Potter^{5,6}, V. Pavlidou^{1,2}, A. Ramaprakash^{2,7,8}, K. Tassis^{1,2}, D. Blinov², S. Kiehlmann², E. Koutsiona¹, S. Maharana⁵, S. Romanopoulos^{1,2}, R. Skalidis⁹, A. Vervelaki¹, S. E. Clark^{10,11}, J. A. Kypriotakis^{1,2}, A. C. S. Readhead^{2,9}

¹ Department of Physics, University of Crete, Vasilika Bouton, 70013 Heraklion, Greece

² Institute of Astrophysics, Foundation for Research and Technology – Hellas, 100 Nikolaou Plastira str. Vassilika Vouton, 70013 Heraklion, Crete, Greece

³ Department of Space, Earth & Environment, Chalmers University of Technology, SE-412 93 Gothenburg, Sweden

⁴ Université Libre de Bruxelles, Science Faculty CP230, B-1050 Brussels, Belgium

⁵ South African Astronomical Observatory, PO Box 9, Observatory, 7935, Cape Town, South Africa

⁶ Department of Physics, University of Johannesburg, PO Box 524, Auckland Park 2006, South Africa

⁷ Cahill Center for Astronomy and Astrophysics, California Institute of Technology, 1216 E California Blvd, Pasadena, CA, 91125, USA

⁸ Inter-University Centre for Astronomy and Astrophysics, Post Bag 4, Ganeshkhind, Pune - 411 007, India

⁹ Owens Valley Radio Observatory, California Institute of Technology, Pasadena, CA, 91125, USA

¹⁰ Department of Physics, Stanford University, Stanford, CA 94305, USA

¹¹ Kavli Institute for Particle Astrophysics & Cosmology, P.O. Box 2450, Stanford University, Stanford, CA 94305, USA

Received – / Accepted –

ABSTRACT

Context. Calibration of optical polarimeters relies on the use of stars with negligible polarization (unpolarized standard stars) for determining the instrumental polarization zero-point. For wide-field polarimeters, calibration is often done by imaging the same star over multiple positions in the field of view - a process which is time-consuming. A more effective technique is to target fields containing multiple standard stars. While this method has been used for fields with highly polarized stars, there are no such sky regions with well-measured unpolarized standard stars.

Aims. We aim to identify sky regions with tens of stars exhibiting negligible polarization, which are suitable for zero-point calibration of wide-field polarimeters.

Methods. We selected stars in regions with extremely low reddening, located at high Galactic latitudes. We targeted four $\sim 40' \times 40'$ fields in the northern, and eight in the southern Equatorial hemisphere. Observations were carried out at the Skinakas Observatory and the South African Astronomical Observatory respectively.

Results. We find two fields in the North and seven in the South with mean polarization lower than $p < 0.1\%$.

Conclusions. At least nine out of twelve fields can be used for zero-point calibration of wide-field polarimeters.

1. Introduction

To date, the development of optical polarimetry instrumentation has primarily emphasized the creation of instruments tailored for single-source observations or with limited field-of-view capabilities. The calibration process for these instruments typically involves utilizing polarimetric standard stars (e.g. Blinov et al. 2023). When there is a need to calibrate the entire field of view, calibration methods often employ techniques such as rastering, where a star of known polarization is placed in different positions of the CCD to assess the instrument-induced polarization variations across the field (e.g. King et al. 2014). This can be very time-consuming and, therefore inefficient for wide field instruments with lots of CCD pixels, especially in the scheme of wide-field surveys.

The domain of optical polarimetry is on the verge of a significant transition as it enters the era of large-area surveys like PASIPHAE (Tassis et al. 2018), SouthPol (Magalhães et al. 2012), and VSTPol (Covino et al. 2020). These surveys will utilize polarimeters equipped with unprecedentedly wide fields of view.

However, the calibration process for these wide-field polarimeters presents a formidable challenge, particularly considering the surveys' aim of achieving high accuracy levels of $p \lesssim 0.1\%$ to fulfill their scientific objectives.

PASIPHAE is a pioneering survey with the primary objective of mapping the polarization of millions of stars located away from the Galactic plane. The scientific goals of the project include the determination of dust cloud distributions and their properties along each line of sight, as well as the investigation of the magnetic field structure within our Galaxy (Pelgrims et al. 2023). Its findings will facilitate the accurate removal of the dust polarization foreground for surveys targeting the detection of the imprint of the primordial polarization B-modes on the cosmic microwave background. (e.g. Polnarev 1985; Kamionkowski et al. 1997). PASIPHAE will utilize two Wide-Area Linear Optical Polarimeters (WALOPs) which will operate from both the southern and northern hemispheres and will be mounted on the South African Astronomical Observatory's (SAAO) 1 m telescope¹, and Skinakas Observatory 1.3 m telescope², respectively. The descrip-

¹ <https://www.sao.ac.za/>

² <https://skinakas.physics.uoc.gr/>

* nmandarakas@physics.uoc.gr

tion of the optical design, expected performance, and overall instrument design can be found in [Maharana et al. \(2020, 2021\)](#).

Given that the targeted accuracy of PASIPHAE in polarization fraction is 0.1%, it is important to calibrate the whole field of view of WALOPs down to this level. [Maharana et al. \(2022\)](#) characterized the magnitude and sources of instrumental polarization and developed an on-sky polarimetric calibration method to obtain the target accuracy for WALOP-South. The calibration model creates an accurate mapping function between the instrument measured, and real Stokes parameters of a target. To develop the calibration model, wide-field sources of known and constant (also referred to as "flat") polarization across the field are observed through the instrument. The corresponding measured polarization values are used to create the mapping functions. One such calibration source is the sky on bright-Moon nights in the vicinity of the Moon. [Patat & Romaniello \(2006\)](#) calibrated the VLT-FORS1 instrument, using the qualitative assumption that the Moon-induced night sky polarization remains fairly constant in scales of a few arcminutes, while [González-Gaitán et al. \(2020\)](#) calibrated the FORS2 instrument by explicitly calculating the polarization of the scattered Moonlight. [Maharana et al. \(2023\)](#) have demonstrated that the sky polarization remains constant at the level of 0.1% or less for fields of size 10 to 20 arcminutes up to 20 degrees away from the Moon, making them suitable "polarimetric flat fields". As shown by [Maharana et al. \(2022\)](#), the polarimetric flat fields suffice for calibration of wide field polarimeters, when used in conjunction with polarimetric standard stars. While polarimetric flat sources allow for relative calibration of the whole field, standard star measurements allow the estimation of the true polarization of the polarimetric flat source, enabling complete and absolute calibration of the entire field of view.

Star fields with uniform polarization across the field can serve as candidate on-sky wide-field calibrators, provided their polarization scatter is smaller than the required calibration accuracy. The advantages of this compared to the full-Moon sky are that (1) it can be carried out on any given night, provided that such a field is available, and (2) it can be used as standard calibrator source whose polarization is known directly from observations, unlike the full-Moon sky, whose polarization can only be calculated based on modelling, or needs multiple observations in different angles from the moon ([González-Gaitán et al. 2020](#)) to achieve a similar result to an observation of a zero-polarized field. This eliminates the need for additional standard star measurements needed to estimate the true polarization of the polarimetric flat source. A major, and often the dominant result of instrumental polarization that wide-field polarimeters suffer from is the polarimetric zero offsets, i.e., the measured Stokes parameters when the observed source is unpolarized. This needs to be corrected using unpolarized wide-field targets. By observing unpolarized targets, one can directly get the polarimetric zero offset, as any potential non-zero cross-talk terms between the Stokes $q = Q/I$ and $u = U/I$ are eliminated. We note that in polarimeters that show non-negligible cross-talk between the linear and circular Stokes parameters, zero-polarization standards are not enough to address this issue. Calibration in these cases would need more extensive modelling ([Wiersema et al. 2018](#)), observations of Stokes V polarization standards ([Giro et al. 2003](#)), and/or in-built calibration sources/devices within the instrument, like in the case of WALOP ([Maharana et al. 2022](#)).

Nonetheless, observations of zero-polarization fields are always essential. To fulfill this missing ingredient for calibrating wide-field polarimeters, in this work we aim to search for zero-polarized patches of the sky that can serve as calibrators for the WALOPs and other wide-field polarimeters. [Skalidis et al.](#)

(2018) surveyed three $15' \times 15'$ regions of the northern sky at high Galactic latitudes with RoboPol, and found one to be consistent with zero polarization, while [Clemens et al. \(2012\)](#) used polarized stellar cluster observations to calibrate the Mimir near-infrared imaging wide-field polarimeter ([Clemens et al. 2007](#)). In order to search for zero-polarized patches, we rely on the known connection between extinction by interstellar dust and observed polarization in a given line-of-sight.

Interstellar dust is ubiquitous in all lines-of-sight (e.g. [Planck Collaboration et al. 2014](#)). Its interaction with the interstellar magnetic field makes interstellar dust clouds act as polarizing filters. Asymmetric interstellar dust grains tend to align their minor axis parallel to the magnetic field lines ([Andersson et al. 2015](#)). Dichroic absorption in optical wavelengths (i.e. the attenuation of the component of the light polarized in the plane-of-the-sky direction of the major axis of the grains) gives rise to dust-induced polarization to originally unpolarized sources behind said dust, with its orientation along the minor axis of the grains, i.e. along the magnetic field lines. In the infrared and sub-mm regime, dust emits thermally, with the emission being polarized along the direction of its major axis, which is perpendicular to the polarization direction observed in the optical. The polarized emission from dust grains has been recently mapped with *Planck* and shown to be well-correlated with the optical starlight polarization ([Planck Collaboration et al. 2020a](#)).

In addition to dust-induced polarization, light passing through the dust suffers from reddening as well. The magnitude of these effects is related to the amount of dust along the line of sight. Empirical investigations have established a relationship between the maximum observed polarization p_{max} and the reddening $E(B-V)$, expressed as $p_{max} = 13\%E(B-V)$ ([Panopoulou et al. 2019](#); [Planck Collaboration et al. 2020a](#)). In this work we use this empirical relation, in conjunction with a publicly available reddening map to identify regions with expected polarization $p \leq 0.1\%$, that could be used as calibrators for wide-field polarimeters. We conducted polarimetric observations in the optical to verify whether these regions are indeed negligibly polarized. In Sect. 2 we describe the sample selection, data acquisition and processing. In Sect. 3 we present the results of the polarization observations. We make our conclusions in Sect. 4, and provide supplementary plots in Appendices A and B.

2. Data

2.1. Sample selection

Our goal is to target regions in the sky with minimal polarization and with an appreciable number of stars that can be used for determining the instrumental zero-point across a field of view of $\sim 40' \times 40'$, which is slightly wider than the field of view of the WALOPs that will be used for PASIPHAE. We are not interested to only find specific zero-polarized stars in wide fields, such as fields with globular or open clusters, (e.g. [Clemens et al. 2012](#)). Such fields may indeed host clusters that are close enough so that their polarization is not affected by the interstellar medium (ISM). However, in these fields there may exist stars outside the cluster that are farther away and well-affected by the ISM. Rather, asserting that a certain region's polarization is minimally affected, ensures that any given star in this region, regardless of distance, or brightness will be suitable for calibration, except for cases of intrinsically polarized stars, which can be easily identified. Thus, the calibration procedure becomes simpler, and stars used for calibration do not necessarily need to be exactly the ones used in this specific work. For example, the use of

other, potentially fainter, sources in our targeted regions would be equally qualified as calibrators, thus making these regions useful for bigger telescopes as well, where bright nearby targets would saturate their cameras.

Existing optical polarization data are sparse at high Galactic latitudes, with a mean density of 0.1 measurements per square degree (Panopoulou et al. 2023). One avenue would be to identify regions with minimal polarized dust emission as observed by *Planck*. However, the *Planck* polarization data are dominated by noise at high Galactic latitudes (Planck Collaboration et al. 2020c,b). Therefore, we searched for the lowest-polarization regions of the sky through reddening, which is an indirect observable of expected polarization levels, as discussed in Sect. 1. We used the Lenz et al. (2017) reddening map, as it is considered the most accurate at high Galactic latitudes (Chiang & Ménard 2019). Based on this map, we selected regions with $E(B - V) < 0.01$ mag, corresponding to a maximum expected polarization fraction of $p_{max} = 0.13\%$, according to the relation $p_{max} = 13\%E(B - V)$ (Panopoulou et al. 2019; Planck Collaboration et al. 2020a). This resulted to 799 square degrees of usable sky area, compared to the total of 16,342 square degrees in the map.

Within the selected area, we searched for $40' \times 40'$ regions which fulfilled the maximum reddening of 0.01 mag criterion across the entire region. We aimed to find fields as spread-out in Right Ascension (RA) as possible, within the visibility constraints of the locations of the PASIPHAE telescopes. This was to ensure that at least one such region is available on any observing night for calibration purposes. However, such regions are not available in a wide range of RAs, as we would wish for. Only 4 regions at northern latitudes and 8 regions at southern latitudes satisfied the aforementioned criteria, which we surveyed. Hereafter, we refer to these regions as "dark patches" (DPN for North, DPS for South).

Within each region, we selected all stars in *Gaia* DR2 (Gaia Collaboration et al. 2016, 2018) (which was the latest available dataset at the time of target selection) with G -band magnitude $G < 14$ mag, to observe as many stars as possible in the least amount of time. Stars that were too bright ($G < 9$ mag) were excluded to avoid saturation on the CCD. We further excluded stars marked as variable in the *Gaia* dataset. Stars with overlapping point-spread-functions as seen in Digital Sky Survey (DSS)³ images of the fields were also excluded, as their polarization could be a result of spurious measurements.

2.2. Data acquisition and reduction - North

In order to acquire data for the dark patch candidates in the northern hemisphere, we utilized the RoboPol instrument, mounted on the Skinakas 1.3 m telescope in Crete, Greece. RoboPol contains no rotating parts and can measure the linear Stokes parameters $q = Q/I$ and $u = U/I$ with a single exposure. Its novel design allows for minimization of systematic and random errors (Ramaprakash et al. 2019). The instrument is optimized for single target measurements in the center of its field of view, where the background noise is minimized with the use of a mask.

We observed four candidate patches between May and November 2021 and June to August 2023. The observations were conducted in Sloan Digital Sky Survey (SDSS)- r' and Johnsons-Cousins R bands. Observations of both bands were considered together, as we have verified with standard stars measurements that these filters are essentially equivalent (Blinov et al. 2023). We selected these filters as the upcoming PASIPHAE survey will

be operating in SDSS- r' . Data reduction and calibration were performed with the standard RoboPol pipeline as outlined in King et al. (2014); Panopoulou et al. (2015); Blinov et al. (2021). Uncertainties of the systematic error are of the order of $\sim 0.1\%$ in the mask of the instrument (Blinov et al. 2023). We note that these uncertainties concern measurements of individual targets. However, when we study a particular field, the accuracy to which we know its mean polarization is dependent on the number of stars observed in that field. The uncertainty of the mean polarization of the field decreases with the number of stars (refer to Eq. 5), and can ultimately be lower than the uncertainty in the polarization of individual targets.

2.3. Data acquisition and reduction - South

All-Stokes photopolarimetry of the Southern dark patches was performed during October of 2021 and August of 2022 on the 1.9-m telescope of the SAAO using HIPPO (Potter et al. 2010). HIPPO's waveplates are contrarotated at 10 Hz and therefore modulate the ordinary and extraordinary beams through the Thompson beamsplitter. The modulation is sufficiently rapid that errors which arise as a result of variable atmospheric conditions or telescope guiding modulations, become minimal. The systematic uncertainty of $\sim 0.1\%$ is estimated from repeating and comparing observations of standards over multiple seasons. The modulated signal is sampled and recorded by two RCA31034A GaAs photomultiplier tubes every millisecond. See Potter et al. (2010) for more details. All measurements were performed with an R filter in the Kron-Cousin system. Polarized and unpolarized standard stars were observed in order to calculate the position angle offsets, instrumental polarization and efficiency factors. Background sky polarization measurements were also taken at frequent intervals during the observations. Data reduction then proceeded as outlined in Potter et al. (2010).

3. Results

All measurements of individual targets are corrected for the instrumental error as

$$q = q^{measured} - q^{inst}, \quad (1)$$

and similarly for u . The uncertainties of the individual targets include the contribution from instrumental error uncertainty. The final uncertainty is calculated as

$$\sigma_q = \sqrt{(\sigma_q^{measured})^2 + (\sigma_q^{inst})^2}, \quad (2)$$

and similarly for u , where the superscripts "measured" and "inst" refer to values obtained from differential photometry and the instrumental error respectively. The instrumental error and its uncertainty is not necessarily identical for Stokes q and u , nor between targets, as it can be time-dependent. The measurements of each targets were corrected using the values of the instrumental error corresponding to the same time period that the targets were observed.

We present the results of the dark patch candidates in Table 1. We present the $q - u$ measurements for DPN1 in Fig. 1, together with their weighted mean, standard deviation, and error on the weighted mean. We also present q , u as a function of distance in the same figure. Distance information was retrieved from the *Gaia* DR3 catalog (Gaia Collaboration et al. 2016, 2023), by inverting the provided parallaxes. If parallax information was not available, we used the distance mentioned in the *distance_gsphot* column

³ <https://archive.eso.org/dss/dss>

of the catalog. Stars with no distance information in either form were not plotted in the figure. Similar plots for all of the fields can be found in Appendix A. The sky location of the dark patches are presented in Fig. 2. Finder charts of the individual stars for which we measured polarization in each region are presented in Appendix B. For each field, we divide the range of RAs and DEC's of our targets in four equal bins. For each bin we calculate and plot the average polarization \bar{p}_{bin} , and its standard deviation. For all of the regions, there is no significant deviation in polarization in any of the bins. Hence, there doesn't exist spatial dependence of the polarization within the fields, and can be considered constant in polarization. Sky maps were obtained from DSS.

Individual stellar measurements of q , u have average statistical uncertainties of $\bar{\sigma}_q = 0.175\%$ and $\bar{\sigma}_u = 0.133\%$ for the northern fields, and $\bar{\sigma}_q = 0.097\%$ and $\bar{\sigma}_u = 0.097\%$ for the southern. However, the values that characterize the average polarization of each field is the weighted mean of the measurements and the error on the weighted mean, $\bar{q} \pm \sigma_{\bar{q}}$ and $\bar{u} \pm \sigma_{\bar{u}}$. Therefore, for each field we calculate the weighted mean of the Stokes parameters as

$$\bar{q} = \frac{\sum_{i=1}^N w_i \cdot q_i}{\sum_{i=1}^N w_i}, \quad (3)$$

i being the individual measurement of each star and N the total number of stars in each field, with $w_i = 1/(\sigma_{q_i})^2$, and σ_{q_i} the uncertainty of the measurement. We are also interested in the weighted standard deviation, defined as

$$q_{std} = \sqrt{\frac{\sum_{i=1}^N w_i \cdot (q_i - \bar{q})^2}{\sum_{i=1}^N w_i}}, \quad (4)$$

and the error of the weighted mean, which, in the case of measurements with different uncertainties, as ours, is

$$\sigma_{\bar{q}} = \frac{1}{\sqrt{\sum_{i=1}^N w_i}}, \quad (5)$$

and similarly for u .

Polarization is a positively defined quantity, expressed as

$$p = \sqrt{q^2 + u^2}, \text{ with its uncertainty } \sigma_p = \sqrt{\frac{q^2 \sigma_q^2 + u^2 \sigma_u^2}{q^2 + u^2}}, \quad (6)$$

with σ_q and σ_u being the uncertainties of q and u respectively. Therefore, measurements are biased towards higher values, especially for low signal-to-noise (S/N) measurements (e.g. [Vailancourt 2006](#)). We debias our measurements using the modified asymptotic (MAS) estimator proposed in [Plaszczynski et al. \(2014\)](#),

$$p_{MAS} = p - \sigma_p^2 \frac{1 - e^{-p^2/\sigma_p^2}}{2p} \quad (7)$$

with p and σ_p as defined in Eq. 6. We present the debiased values in Table 1. Conversely, the bias in the polarization angle is likely very small ([Montier et al. 2015](#)). Thus the expression of the polarization angle $\chi = \frac{1}{2} \arctan(\frac{u}{q})$ was used without correction.

The observed polarization of stars in any given field is expected to arise solely due to dichroic absorption of the light by aligned dust grains as discussed in Sect. 1. This is based on the fact that most stars are intrinsically unpolarized with the possible exceptions of magnetic stars, or stars surrounded by dusty disks

([Fadeyev 2007](#); [Clarke 2010](#)). The potential existence of such stars in our samples would manifest as clear outliers in the $q - u$ plots. For each of our patches, we performed a $3-\sigma$ clipping three times, to discard outliers. This process excluded only 1 star from DPN3, and 1 star from DPS7, while the number of the remaining stars per patch ranges between 16 and 37.

The observed scatter between the measurements of different stars in the same region is a combination of the intrinsic scatter of the sources within the region and the statistical scatter introduced by the instrument, arising from photon noise and instrumental systematics. That is

$$\sigma_q^{observed} = \sqrt{(\sigma_q^{intrinsic})^2 + (\sigma_q^{statistical})^2}, \quad (8)$$

and similar for u , with the assumption that these sources of variance are Gaussian. The statistical scatter of both the northern and the southern instruments used for this study is of the order of $\sim 0.1\%$, as deduced by standards observations. Therefore, the intrinsic scatter in the polarization of the observed patches is maximum 0.1% for all cases.

4. Discussion

We have identified and surveyed twelve regions of the sky, with very low extinction values, to assess whether they exhibit significantly low polarization, to be used as calibrators for wide-field polarimeters. We measured the linear polarization of stars in four patches in the northern, and eight in the southern hemisphere. We find that two regions in the North and seven in the South display mean polarization of $\bar{p} < 0.1\%$, while one more in each hemisphere has a mean polarization marginally above 0.1% . Moreover, we have included the regions probed by [Skalidis et al. \(2018\)](#) in Table 1 as one of those regions could also serve as a zero-polarization calibrator.

At high Galactic latitudes (as are the regions in our study) the full column density, as well as the dust polarization in emission and absorption, is dominated by the wall of the Local Bubble located between 150 and 300 pc from the Sun ([Skalidis & Pelgrims 2019](#); [Pelgrims et al. 2020](#)). Most of the observed stars in our samples have distances larger than that. Therefore, we are confident that our stellar polarization measurements sample all the dust column that could induce polarization along the line of sight of the regions surveyed (see plots in Appendix A). Moreover, we do not notice any significant change of the measured polarization as a function of distance. In conclusion, our measurements are characteristic of each field, regardless of distance, and represent the true polarization value arising due to the effect of interstellar dust in each region.

An interesting outcome of this study is the mean polarization of DPN1. Based on its reddening value from [Lenz et al. \(2017\)](#) $E(B - V) \sim 0.06$ mag, and the relation $p_{max} = 13\%E(B - V)$, we would not expect its polarization to be at the measured value $p = 0.283 \pm 0.029\%$. This could be due to reasons related to how the dust maps are constructed, and their uncertainties. There is quite high uncertainty in modelling that is associated with dust maps at high latitude. For example, [Lenz et al. \(2017\)](#) compared the [Schlegel et al. \(1998\)](#) maps with H_1 data ([HI4PI Collaboration et al. 2016](#)) to derive the reddening $E(B - V)$. This technique of modelling involves uncertainties relating to two factors: i) The gas to dust ratio, which may exhibit variations across the sky ([Shull & Panopoulou 2023](#); [Skalidis et al. 2023](#)) and ii) the dust modeling, which results in important differences at high latitudes ([Chiang & Ménard 2019](#); [Chiang 2023](#)). Characteristic evidence for the

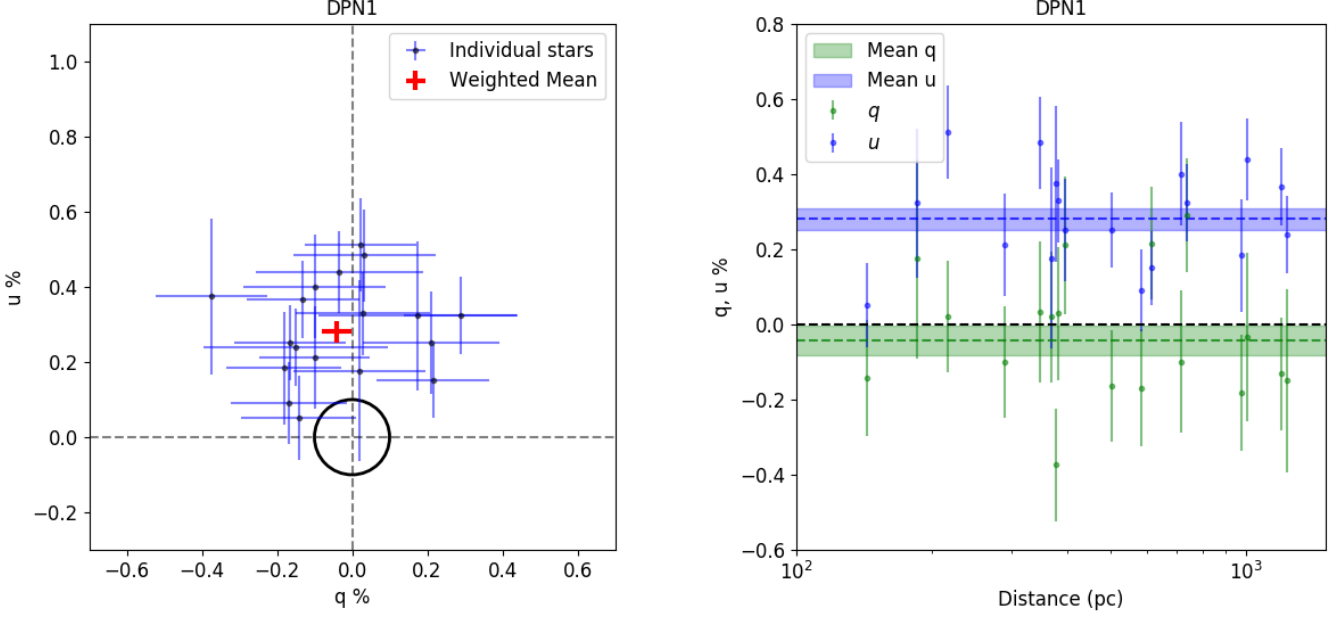


Fig. 1: Left: $q - u$ measurements of individual stars of DPN1 (blue), together with the weighted mean and the error on the weighted mean (red). The black circle marks the value $p = 0.1\%$. Right: q (green) and u (blue) measurements of the stars in the patch as a function of the distance from Earth. The green (blue) dashed line corresponds to the weighted mean q (u) of the patch and the green (blue) shaded region to its error on the weighted mean.

Table 1: Properties of the dark patch candidates.

Notes. \bar{p} and $\sigma_{\bar{p}}$ correspond to the debiased estimate of the mean polarization, and its error respectively. $\bar{\chi}$ and $\sigma_{\bar{\chi}}$ are similar for the polarization angle. \bar{q} , q_{std} , and $\sigma_{\bar{q}}$ are the weighted mean of q values, its standard deviation, and error on the mean respectively. Similar for u . Empty cells correspond to information that is not available.

Name	N_{stars}	RA (deg)	DEC (deg)	\bar{p} (%)	$\sigma_{\bar{p}}$ (%)	$\bar{\chi}$ (°)	$\sigma_{\bar{\chi}}$ (°)	\bar{q} (%)	q_{std} (%)	$\sigma_{\bar{q}}$ (%)	\bar{u} (%)	u_{std} (%)	$\sigma_{\bar{u}}$ (%)
North													
DPN1	17	246.7065	44.0438	0.283	0.029	49.236	3.268	-0.042	0.179	0.039	0.282	0.134	0.029
DPN2	25	165.3404	59.5480	0.105	0.026	31.952	8.513	0.048	0.202	0.032	0.098	0.140	0.025
DPN3	16	220.4940	59.9686	0.058	0.041	82.982	22.315	-0.068	0.177	0.041	0.017	0.102	0.032
DPN4	36	160.4000	56.6931	0.059	0.021	54.363	10.829	-0.020	0.104	0.025	0.059	0.103	0.020
South													
DPS1	29	59.1394	-45.6599	0.093	0.018	36.449	6.675	0.028	0.098	0.018	0.091	0.119	0.018
DPS2	37	342.303	-47.6786	0.123	0.014	-43.864	6.829	0.005	0.086	0.014	-0.126	0.134	0.014
DPS3	25	70.4262	-53.1910	0.039	0.019	26.565	18.178	0.027	0.093	0.019	0.036	0.145	0.019
DPS4	23	53.0764	-28.4748	0.047	0.020	42.145	12.009	0.005	0.110	0.020	0.050	0.115	0.020
DPS5	22	343.9268	-51.2097	0.049	0.020	-70.166	12.772	-0.041	0.098	0.020	-0.034	0.090	0.020
DPS6	26	345.6808	-51.7997	0.049	0.018	-63.652	12.131	-0.032	0.114	0.018	-0.042	0.102	0.018
DPS7	25	342.3994	-49.7344	0.024	0.020	-63.435	24.630	-0.018	0.117	0.020	-0.024	0.090	0.020
DPS8	24	340.8273	-49.0403	0.069	0.019	-65.817	9.862	-0.048	0.106	0.019	-0.054	0.119	0.019
Dark Patches of Skalidis et al. (2018)													
DP1	24	191.2318	57.1060	0.0	0.038	41	22	0.007		0.041	0.053		0.037
DP2	23	150.7294	54.4580	0.107	0.036	18	9	0.091		0.036	0.066		0.036
DP3	21	144.9987	34.1192	0.203	0.044	6	5	0.203		0.045	0.045		0.037

high uncertainties in dust maps, is the differences between maps, especially in high latitudes. For instance, while the reddening value for DPN1 from Lenz et al. (2017) is $E(B - V) \sim 0.06$ mag, the corresponding value derived from the Planck Collaboration et al. (2016) map is $E(B - V) \sim 0.013$ mag. At the same time, the stellar reddening based maps (e.g. Green et al. 2019) have

statistical uncertainties that are comparable to the extinction, so they too cannot be trusted on a pixel-by-pixel basis. Having discussed that, it is worth mentioning that the recent work of Angarita et al. (2023) place higher constraints in the relation $p_{max}/E(B - V)$, finding an upper limit of $p_{max} \sim 16\%E(B - V)$ in intermediate latitudes $|b| > 7.5$ deg. Therefore, the extraordinary

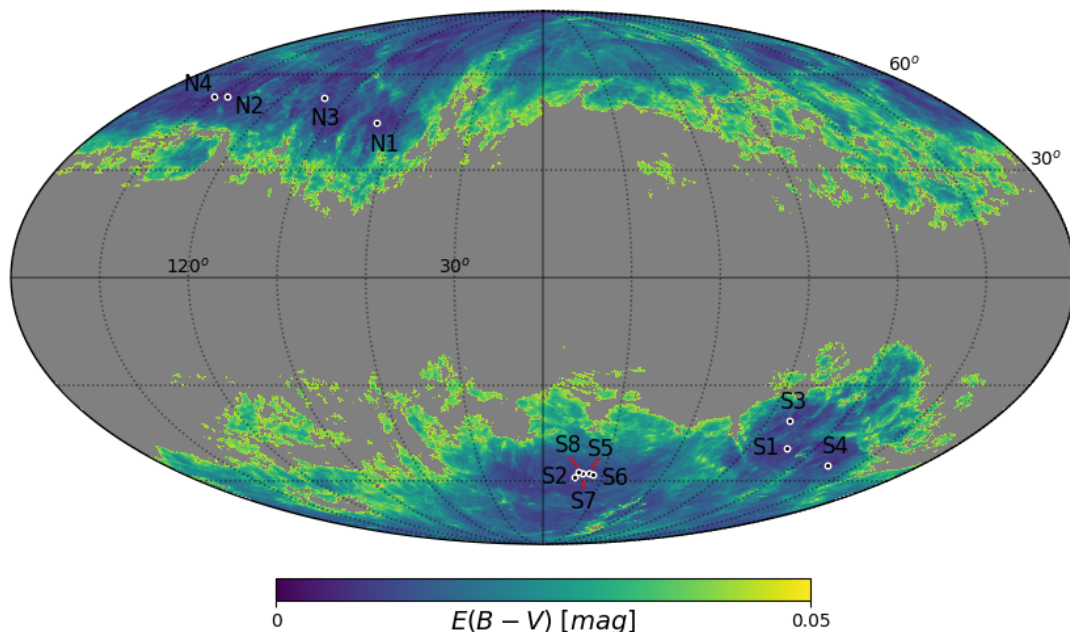


Fig. 2: Locations of the regions surveyed in this work (white circles), overlplotted on the [Lenz et al. \(2017\)](#) extinction map. The map is in Galactic coordinates, centered on $l, b = (0,0)$ in Mollweide projection. Circles size is arbitrary. The red segments are used to distinguish between closely located fields. We use "N" instead of "DPN", and "S" instead of "DPS" for clarity.

value in the mean polarization of DPN1 seems to be mostly associated with the uncertainty of the extinction of the field, but it is not impossible that it is an outlier in the $p_{max}/E(B-V)$ relation.

In conclusion, the most important aspect of this work is that all fields, even the ones with $\bar{p} > 0.1\%$, display very low intrinsic scatter in polarization ($< 0.1\%$). Thus, they can be considered as polarimetric standard fields. Depending on the needs and aims in accuracy of different polarization surveys and instruments, we expect that between 9 and all of the surveyed regions could be used as zero-polarization calibrators for wide-field polarimeters.

All data will become publicly available on CDS.

Acknowledgements. The authors thank A. Steiakaki for useful discussions. We acknowledge the assistance of the anonymous referee who helped make this manuscript better. The PASIPHAE program is supported by grants from the European Research Council (ERC) under grant agreements No. 771282 and No. 772253; by the National Science Foundation (NSF) award AST-2109127; by the National Research Foundation of South Africa under the National Equipment Programme; by the Stavros Niarchos Foundation under grant PASIPHAE; and by the Infosys Foundation. VPa and SR acknowledge support by the Hellenic Foundation for Research and Innovation under the "First Call for H.F.R.I. Research Projects to support Faculty members and Researchers and the procurement of high-cost research equipment grant", Project 1552 CIRCE, and by the Foundation of Research and Technology – Hellas Synergy Grants Program (project MagMASim) VPe acknowledges funding from a Marie Curie Action of the European Union (grant agreement No. 101107047). This work was supported by NSF grant AST-2109127. The Digitized Sky Surveys were produced at the Space Telescope Science Institute under U.S. Government grant NAG W-2166. The images of these surveys are based on photographic data obtained using the Oschin Schmidt Telescope on Palomar Mountain and the UK Schmidt Telescope. The plates were processed into the present compressed digital form with the permission of these institutions. This work has made use of data from the European Space Agency (ESA) mission *Gaia* (<https://www.cosmos.esa.int/gaia>), processed by the *Gaia* Data Processing and Analysis Consortium (DPAC, <https://www.cosmos.esa.int/web/gaia/dpac/consortium>). Funding for the DPAC has been provided by national institutions, in particular the institutions participating in the *Gaia* Multilateral Agreement.

References

- Andersson, B. G., Lazarian, A., & Vaillancourt, J. E. 2015, *ARA&A*, 53, 501
 Angarita, Y., Versteeg, M. J. F., Haverkorn, M., et al. 2023, *AJ*, 166, 34
 Blinov, D., Kiehlmann, S., Pavlidou, V., et al. 2021, *MNRAS*, 501, 3715
 Blinov, D., Maharana, S., Bouzelou, F., et al. 2023, *A&A*, 677, A144
 Chiang, Y.-K. 2023, *ApJ*, 958, 118
 Chiang, Y.-K. & Ménard, B. 2019, *ApJ*, 870, 120
 Clarke, D. 2010, *Stellar Polarimetry*
 Clemens, D. P., Pinnick, A. F., & Pavel, M. D. 2012, *ApJS*, 200, 20
 Clemens, D. P., Sarcia, D., Grabau, A., et al. 2007, *PASP*, 119, 1385
 Covino, S., Smette, A., & Snik, F. 2020, in *VST Beyond 2021*, 20
 Fadeyev, Y. A. 2007, *Astronomy Letters*, 33, 103
 Gaia Collaboration, Brown, A. G. A., Vallenari, A., et al. 2018, *A&A*, 616, A1
 Gaia Collaboration, Prusti, T., de Bruijne, J. H. J., et al. 2016, *A&A*, 595, A1
 Gaia Collaboration, Vallenari, A., Brown, A. G. A., et al. 2023, *A&A*, 674, A1
 Giro, E., Bonoli, C., Leone, F., et al. 2003, in *Society of Photo-Optical Instrumentation Engineers (SPIE) Conference Series*, Vol. 4843, *Polarimetry in Astronomy*, ed. S. Fineschi, 456–464
 González-Gaitán, S., Mourão, A. M., Patat, F., et al. 2020, *A&A*, 634, A70
 Green, G. M., Schlafly, E., Zucker, C., Speagle, J. S., & Finkbeiner, D. 2019, *ApJ*, 887, 93
 HI4PI Collaboration, Ben Bekhti, N., Flöer, L., et al. 2016, *A&A*, 594, A116
 Kamionkowski, M., Kosowsky, A., & Stebbins, A. 1997, *Phys. Rev. D*, 55, 7368
 King, O. G., Blinov, D., Ramaprakash, A. N., et al. 2014, *MNRAS*, 442, 1706
 Lenz, D., Hensley, B. S., & Doré, O. 2017, *ApJ*, 846, 38
 Magalhães, A. M., de Oliveira, C. M., Carciofi, A., et al. 2012, *AIP Conference Proceedings*, 1429, 244
 Maharana, S., Anche, R. M., Ramaprakash, A. N., et al. 2022, *Journal of Astronomical Telescopes, Instruments, and Systems*, 8, 038004
 Maharana, S., Kiehlmann, S., Blinov, D., et al. 2023, *A&A*, 679, A68
 Maharana, S., Kypriotakis, J. A., Ramaprakash, A. N., et al. 2020, in *Society of Photo-Optical Instrumentation Engineers (SPIE) Conference Series*, Vol. 11447, *Ground-based and Airborne Instrumentation for Astronomy VIII*, ed. C. J. Evans, J. J. Bryant, & K. Motohara, 114475E
 Maharana, S., Kypriotakis, J. A., Ramaprakash, A. N., et al. 2021, *Journal of Astronomical Telescopes, Instruments, and Systems*, 7, 014004
 Montier, L., Plaszczynski, S., Levrier, F., et al. 2015, *A&A*, 574, A136
 Panopoulou, G., Tassis, K., Blinov, D., et al. 2015, *MNRAS*, 452, 715
 Panopoulou, G. V., Hensley, B. S., Skalidis, R., Blinov, D., & Tassis, K. 2019, *A&A*, 624, L8
 Panopoulou, G. V., Markopouloti, L., Bouzelou, F., et al. 2023, *arXiv e-prints*, arXiv:2307.05752

- Patat, F. & Romaniello, M. 2006, *PASP*, 118, 146
- Pelgrims, V., Ferrière, K., Boulanger, F., Lallement, R., & Montier, L. 2020, *A&A*, 636, A17
- Pelgrims, V., Panopoulou, G. V., Tassis, K., et al. 2023, *A&A*, 670, A164
- Planck Collaboration, Abergel, A., Ade, P. A. R., et al. 2014, *A&A*, 571, A11
- Planck Collaboration, Aghanim, N., Akrami, Y., et al. 2020a, *A&A*, 641, A12
- Planck Collaboration, Aghanim, N., Akrami, Y., et al. 2020b, *A&A*, 641, A3
- Planck Collaboration, Aghanim, N., Ashdown, M., et al. 2016, *A&A*, 596, A109
- Planck Collaboration, Akrami, Y., Argüeso, F., et al. 2020c, *A&A*, 641, A2
- Plaszczynski, S., Montier, L., Levrier, F., & Tristram, M. 2014, *MNRAS*, 439, 4048
- Polnarev, A. G. 1985, *Soviet Ast.*, 29, 607
- Potter, S. B., Buckley, D. A. H., O'Donoghue, D., et al. 2010, *MNRAS*, 402, 1161
- Ramaprakash, A. N., Rajarshi, C. V., Das, H. K., et al. 2019, *MNRAS*, 485, 2355
- Schlegel, D. J., Finkbeiner, D. P., & Davis, M. 1998, *ApJ*, 500, 525
- Shull, J. M. & Panopoulou, G. V. 2023, arXiv e-prints, arXiv:2310.12205
- Skalidis, R., Golsmith, P. F., Hopkins, P. F., & Ponnada, S. B. 2023, arXiv e-prints, arXiv:2312.02274
- Skalidis, R., Panopoulou, G. V., Tassis, K., et al. 2018, *A&A*, 616, A52
- Skalidis, R. & Pelgrims, V. 2019, *A&A*, 631, L11
- Tassis, K., Ramaprakash, A. N., Readhead, A. C. S., et al. 2018, arXiv e-prints, arXiv:1810.05652
- Vaillancourt, J. E. 2006, *PASP*, 118, 1340
- Wiersema, K., Higgins, A. B., Covino, S., & Starling, R. L. C. 2018, *PASA*, 35, e012

Appendix A: Polarization measurements of the observed fields

We present here our measurements of all of the dark patches, similarly to Fig. 1.

Appendix B: Finder charts of stars in the observed fields

In this appendix we present the sky maps of the dark patches, where we mark the observed stars. We also plot the dependence of the average polarization between different slices of RA and DEC of the same field, to examine the presence of any spatial dependence of the polarization within the field.

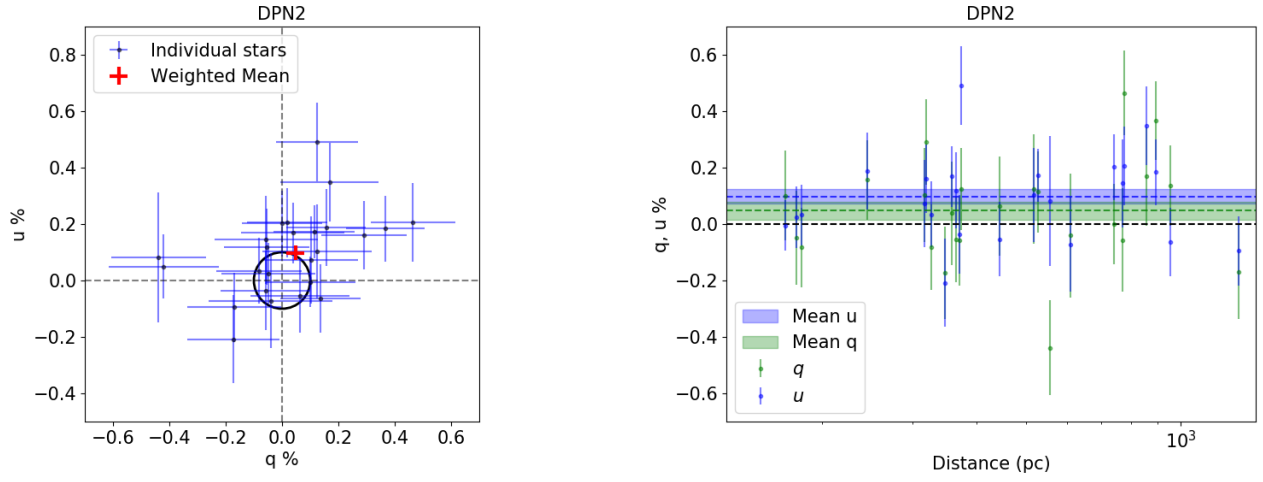


Fig. A.1: Same as Fig. 1 but for DPN2.

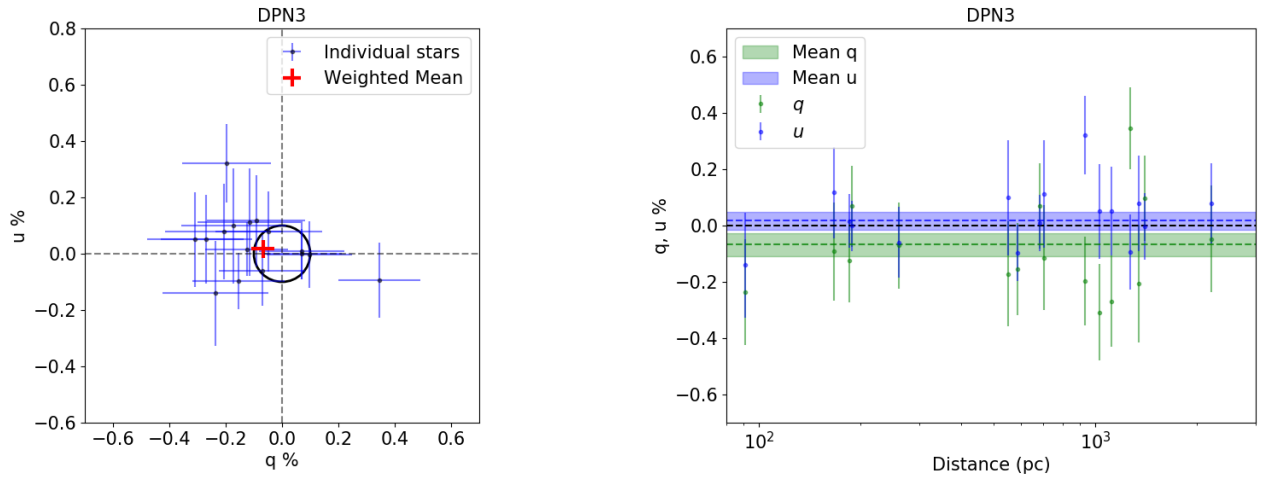


Fig. A.2: Same as Fig. 1 but for DPN3.

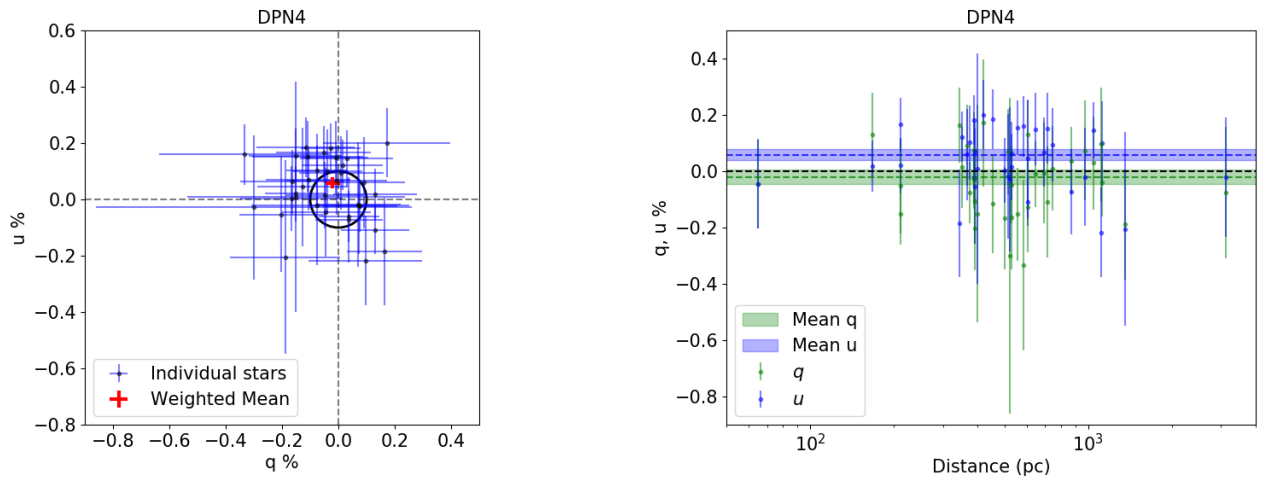


Fig. A.3: Same as Fig. 1 but for DPN4.

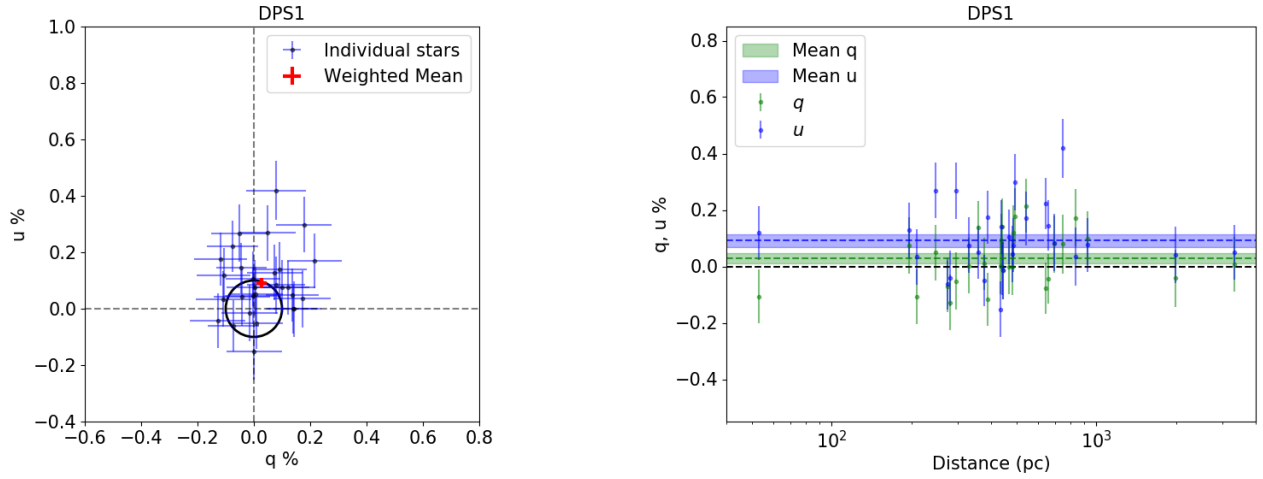


Fig. A.4: Same as Fig. 1 but for DPS1.

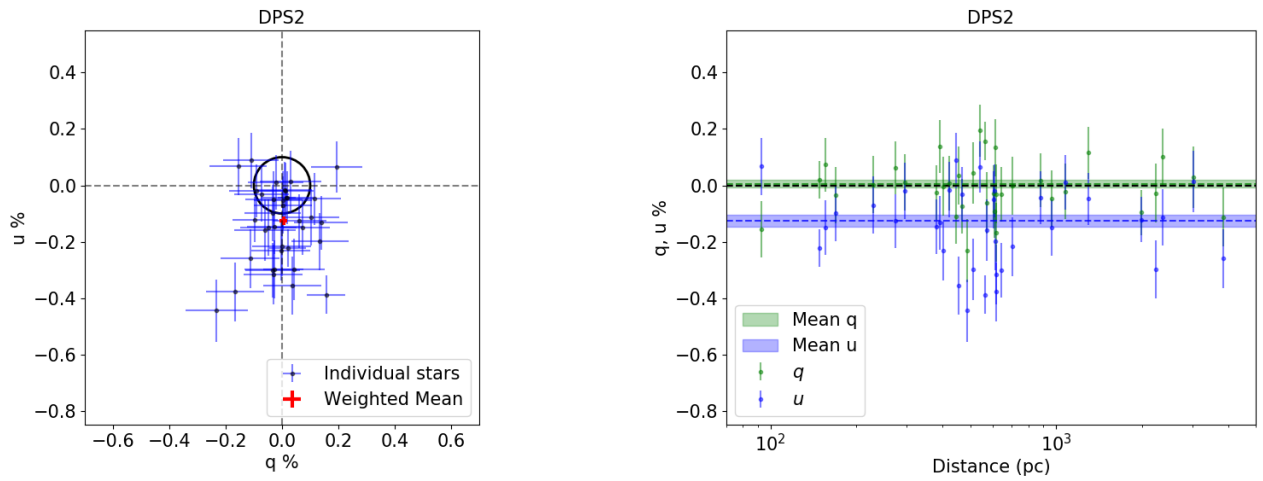


Fig. A.5: Same as Fig. 1 but for DPS2.

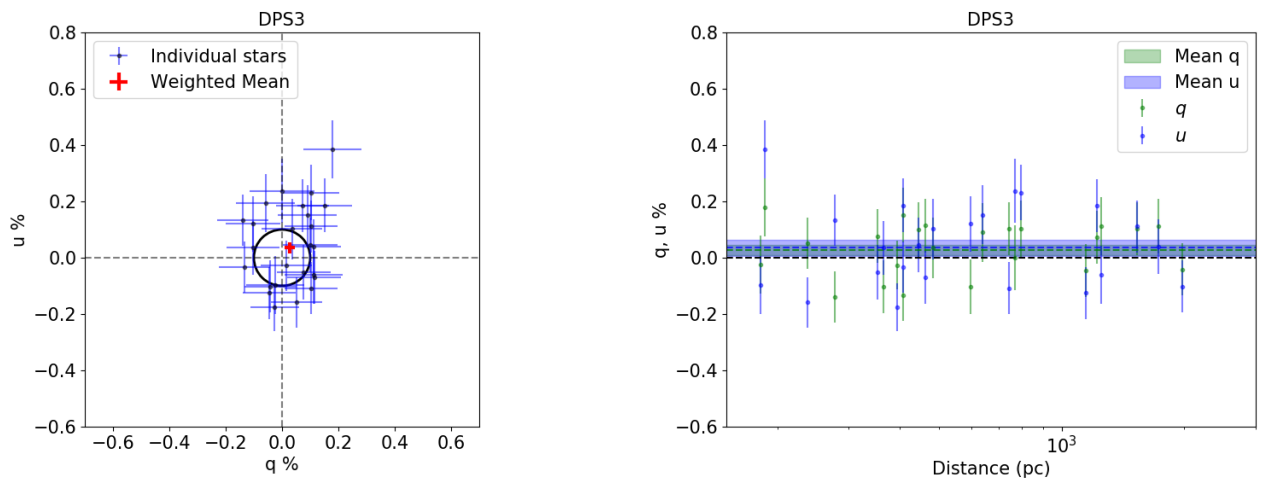


Fig. A.6: Same as Fig. 1 but for DPS3.

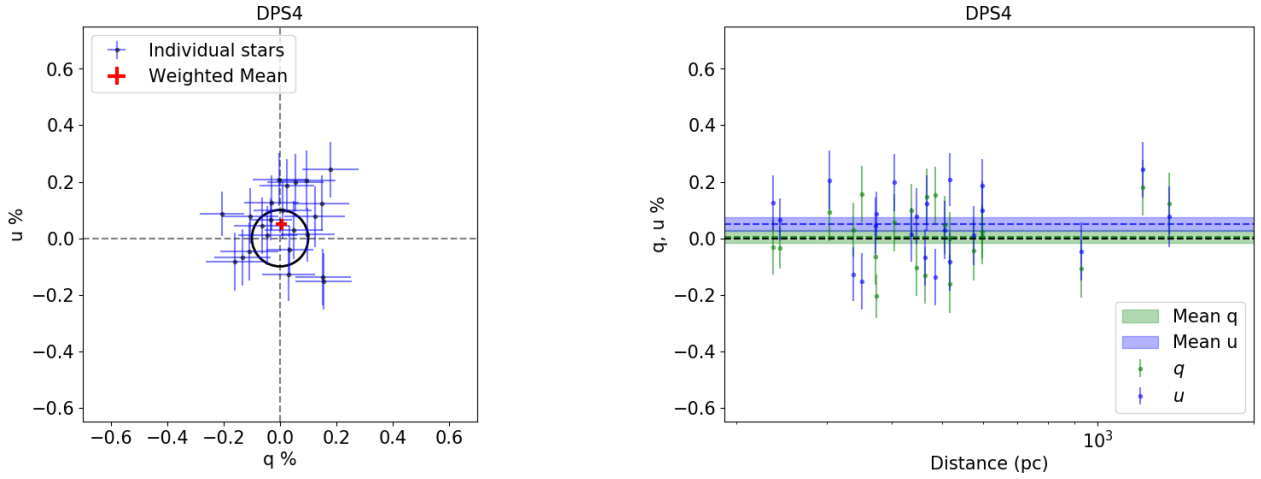


Fig. A.7: Same as Fig. 1 but for DPS4.

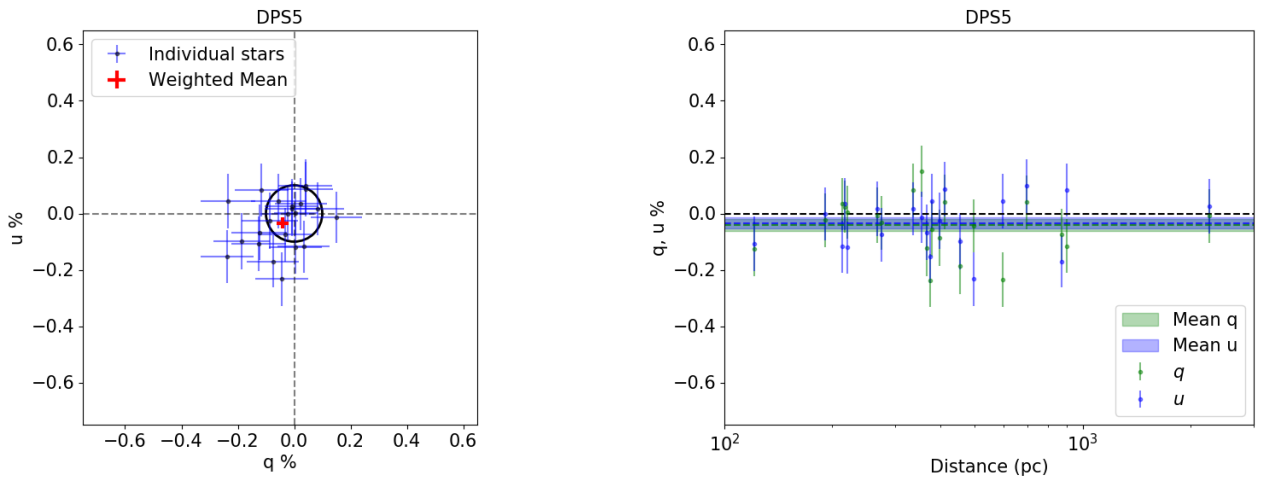


Fig. A.8: Same as Fig. 1 but for DPS5.

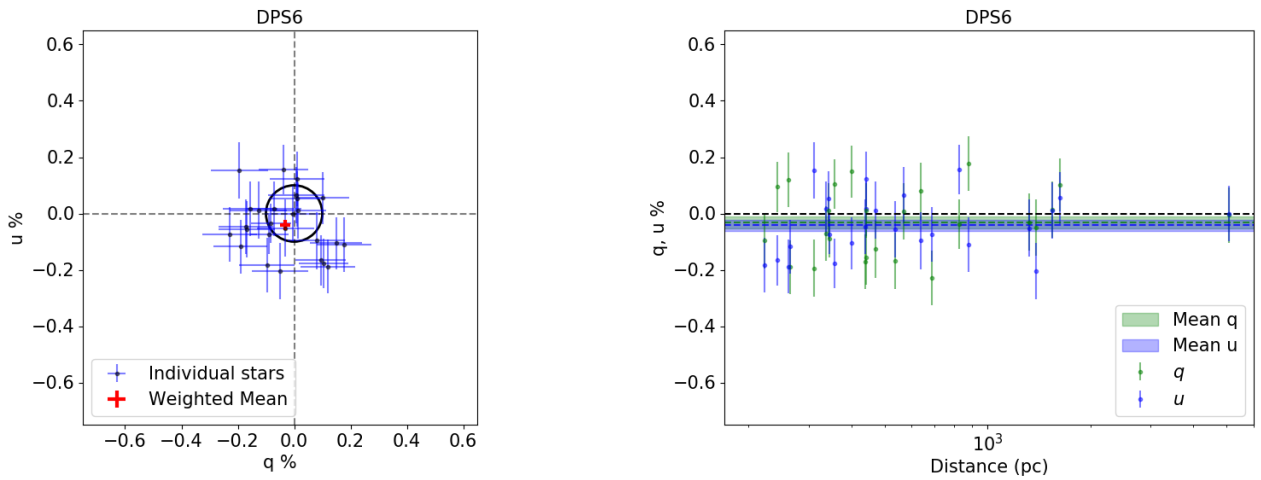


Fig. A.9: Same as Fig. 1 but for DPS6.

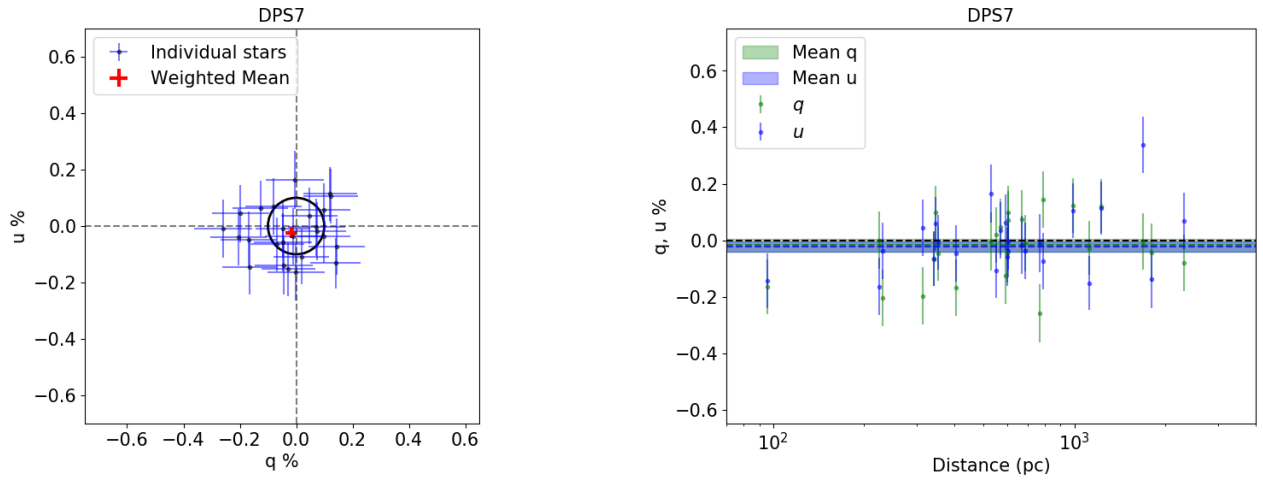


Fig. A.10: Same as Fig. 1 but for DPS7.

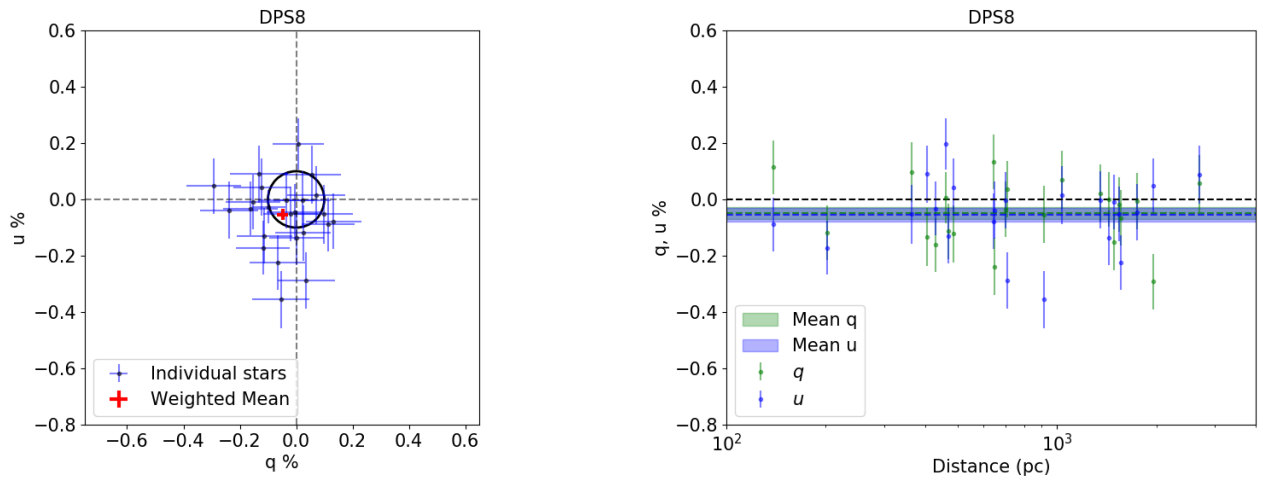


Fig. A.11: Same as Fig. 1 but for DPS8.

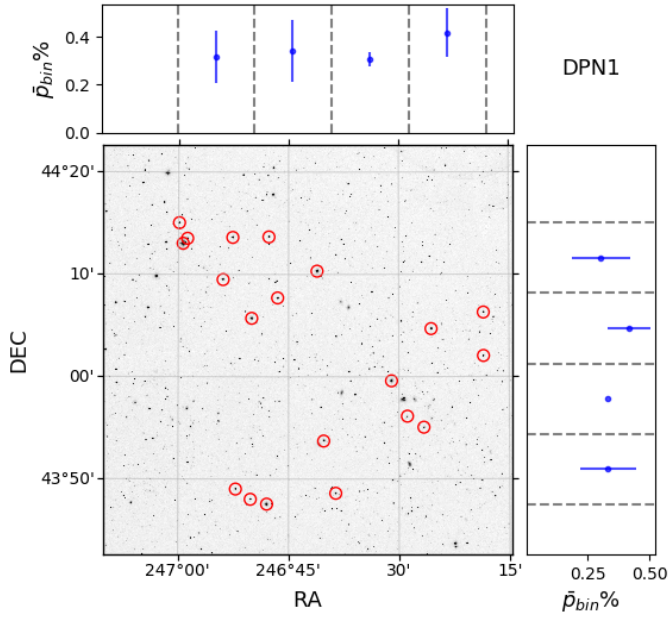


Fig. B.1: Observed stars in DPN1, marked with red circles. The RA and DEC range of the targets are divided in four equal bins. The blue points correspond to the average polarization of the stars within each bin. Errorbars represent the standard deviation of polarization measurements within each bin.

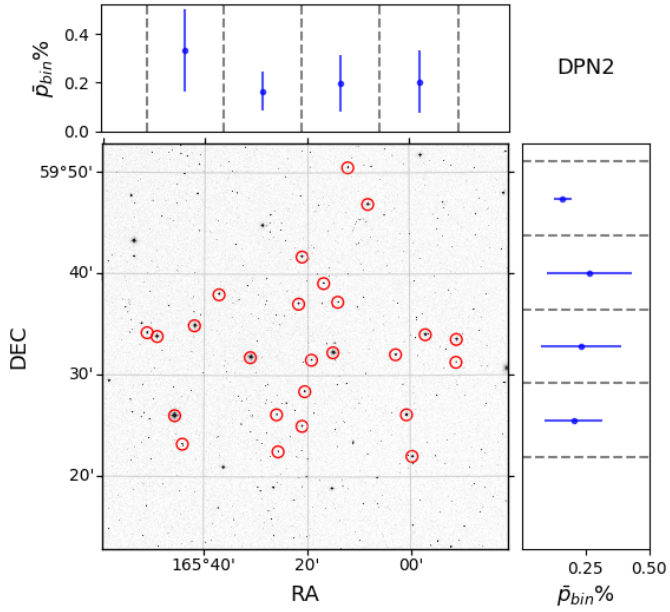


Fig. B.2: Same as Fig. B.1 but for DPN2.

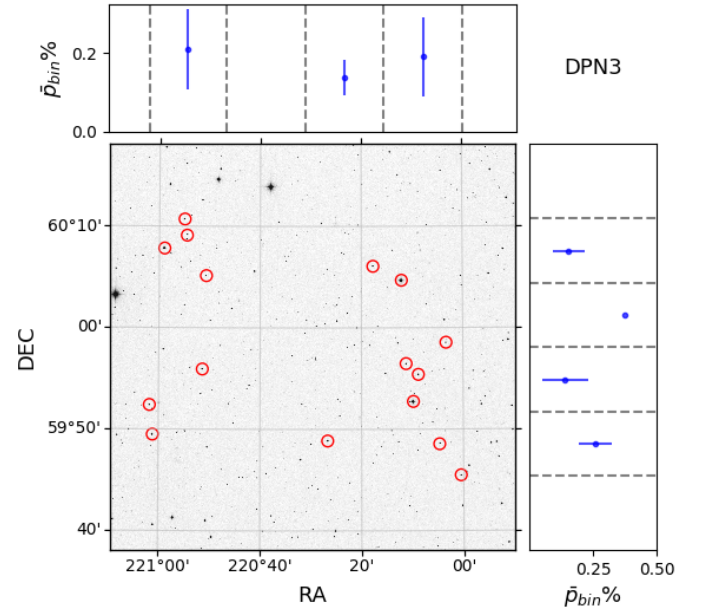


Fig. B.3: Same as Fig. B.1 but for DPN3.

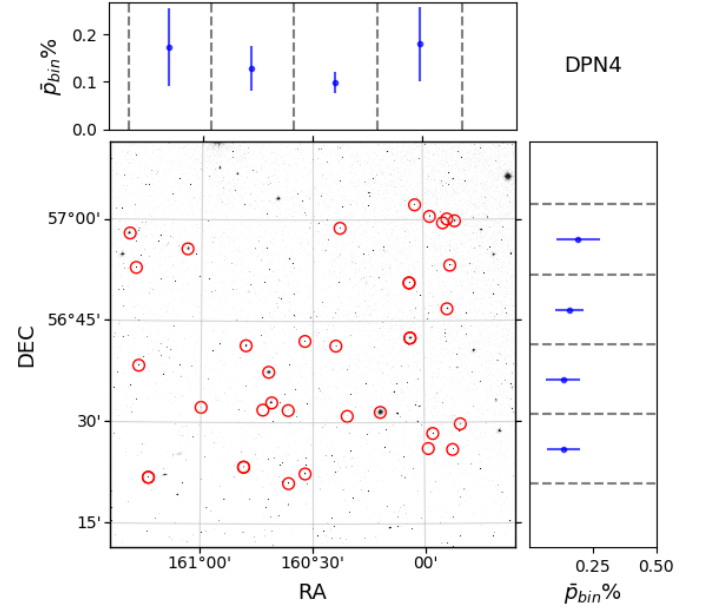


Fig. B.4: Same as Fig. B.1 but for DPN4.

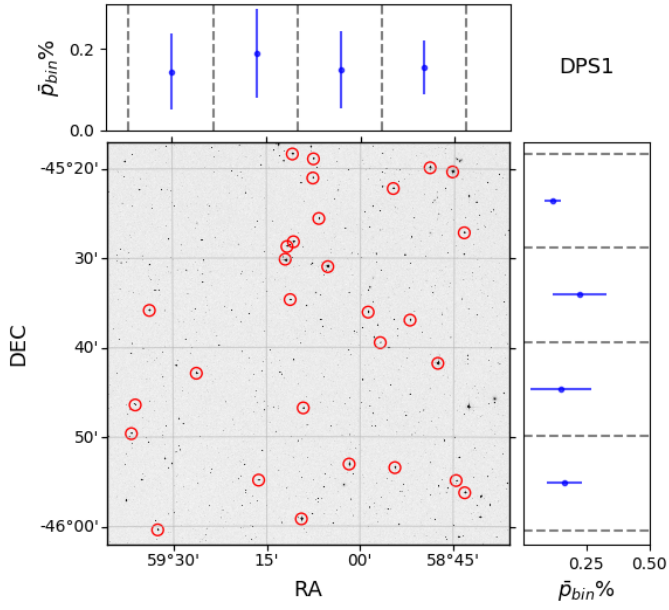


Fig. B.5: Same as Fig. B.1 but for DPS1.

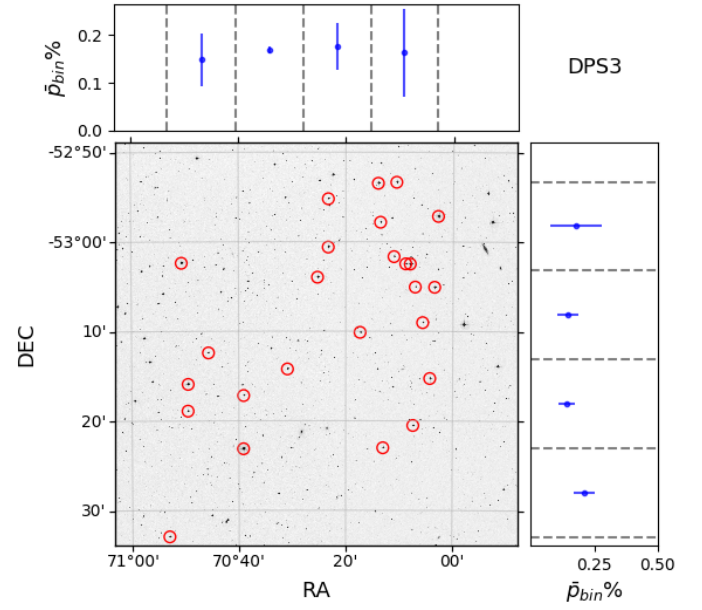


Fig. B.7: Same as Fig. B.1 but for DPS3.

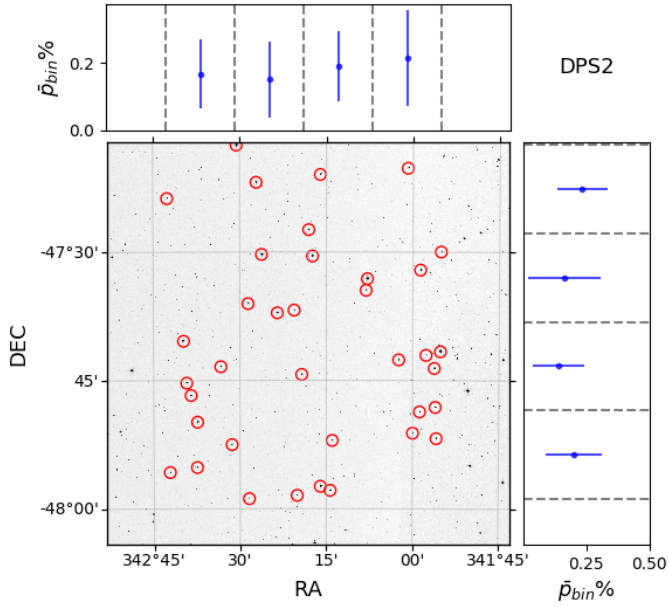


Fig. B.6: Same as Fig. B.1 but for DPS2.

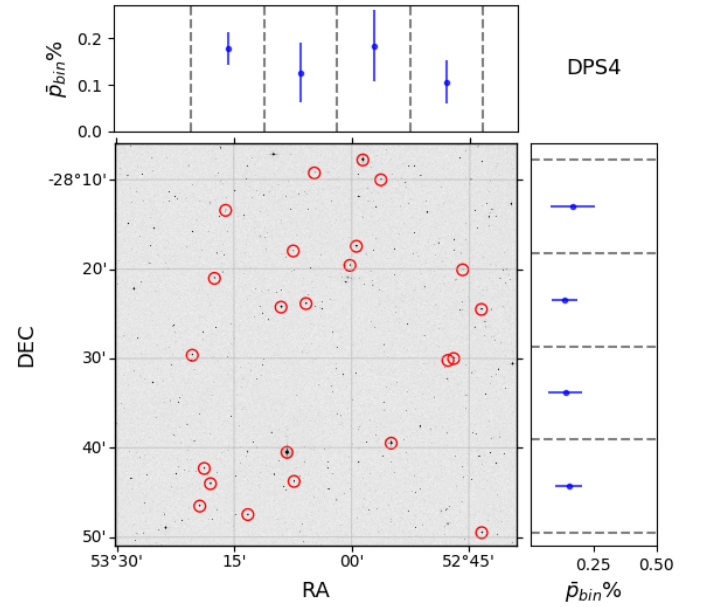


Fig. B.8: Same as Fig. B.1 but for DPS4.

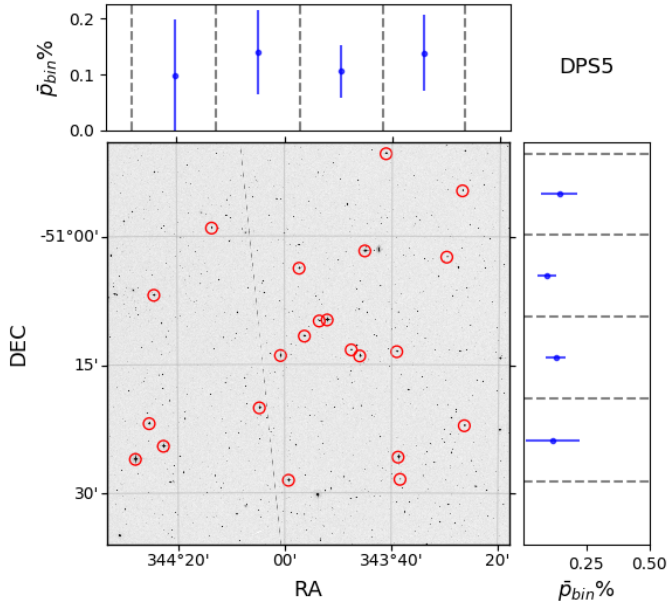


Fig. B.9: Same as Fig. B.1 but for DPS5.

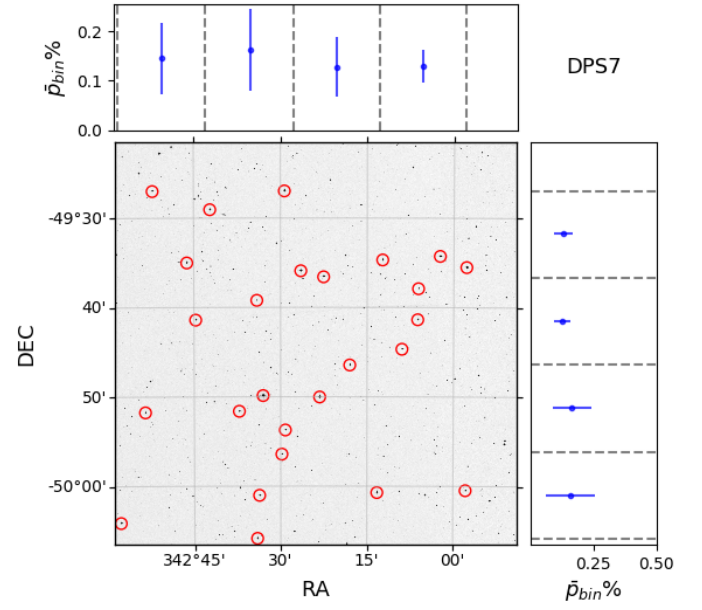


Fig. B.11: Same as Fig. B.1 but for DPS7.

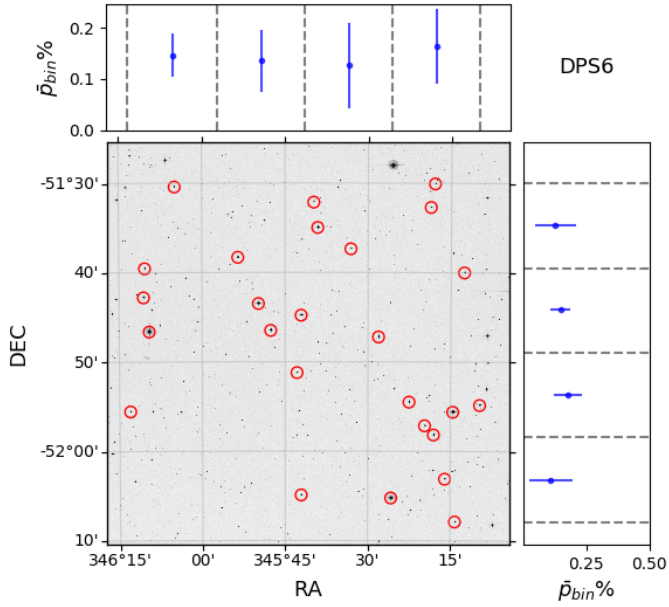


Fig. B.10: Same as Fig. B.1 but for DPS6.

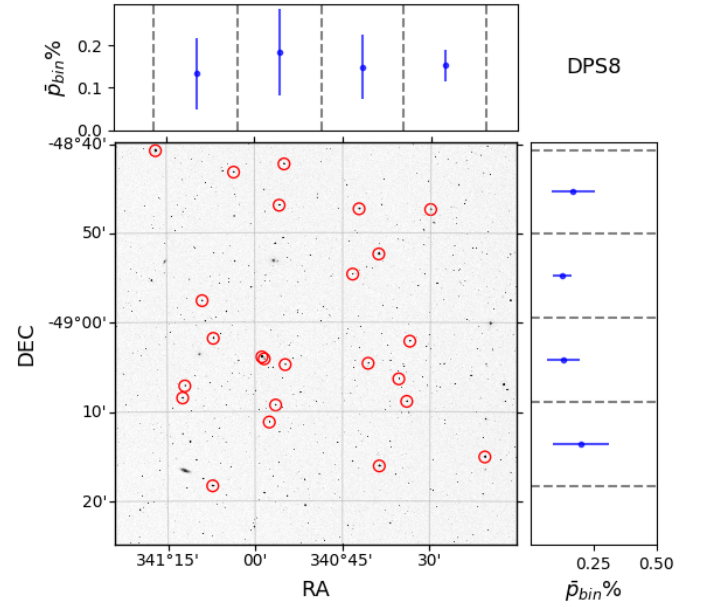


Fig. B.12: Same as Fig. B.1 but for DPS8.